

Article

Open Access



Scissor g-C₃N₄ for high-density loading of catalyst domains in mesoporous thin-layer conductive network for durable Li-S batteries

Chuanzhong Lai^{1,2,3,#}, Xuejun Zhou^{1,3,#}, Meng Lei^{1,3}, Wenlong Liu^{1,2,3}, Xiaoke Mu⁴, Chilin Li^{1,2,3,*}

¹State Key Laboratory of High Performance Ceramics and Superfine Microstructure, Shanghai Institute of Ceramics, Chinese Academy of Sciences, Shanghai 201899, China.

²Center of Materials Science and Optoelectronics Engineering, University of Chinese Academy of Sciences, Beijing 100049, China.

³CAS Key Laboratory of Materials for Energy Conversion, Shanghai Institute of Ceramics, Chinese Academy of Sciences, Shanghai 201899, China.

⁴Institute of Nanotechnology (INT), Karlsruhe Institute of Technology, Eggenstein-Leopoldshafen 76344, Germany.

#Authors contributed equally.

*Correspondence to: Prof. Chilin Li, State Key Laboratory of High Performance Ceramics and Superfine Microstructure, Shanghai Institute of Ceramics, Chinese Academy of Sciences, 585 He Shuo Road, Shanghai 201899, China. E-mail: chilinli@mail.sic.ac.cn

How to cite this article: Lai C, Zhou X, Lei M, Liu W, Mu X, Li C. Scissor g-C₃N₄ for high-density loading of catalyst domains in mesoporous thin-layer conductive network for durable Li-S batteries. *Energy Mater* 2023;3:300025.

<https://dx.doi.org/10.20517/energymater.2023.02>

Received: 18 Jan 2023 **First Decision:** 28 Feb 2023 **Revised:** 19 Apr 2023 **Accepted:** 8 May 2023 **Published:** 29 May 2023

Academic Editors: Yuping Wu, Jia-Qi Huang **Copy Editor:** Fangling Lan **Production Editor:** Fangling Lan

Abstract

The application of Li-S batteries (LSBs) is hindered by the undesired shuttle effect that leads to the fast consumption of active materials. The separator modification by using the carbon matrix with embedded metal nitride as catalyst can ease the problem. However, the previous synthesis processes of metal nitride catalysts are difficult to achieve a balance between their high-density production, homogenous distribution and excellent electronic contact with conductive substrates. Herein, we propose a bond scissoring strategy based on g-C₃N₄ to prepare NbN catalyst domains with high-density loading uniformly embedded in mesoporous thin-layer conductive carbon network (NbN/C) for durable LSBs. The molten salt reaction process is favorable for the diffusion of Nb cations into a porous g-C₃N₄ precursor to break the C-N bond and immobilize the N element. The residual monolithic carbon framework with space confinement effect limits the irregular growth and stacking of NbN precipitates. The NbN catalytic domains exhibit a strong adsorption effect on lithium polysulfides (LiPSs) and accelerate their liquid-solid conversion reactions. The LSBs utilizing an NbN/C-modified separator show superior cycling and rate performance, with a high-capacity retention of 72.7% after 1,000 cycles under 2 C and a high areal



© The Author(s) 2023. **Open Access** This article is licensed under a Creative Commons Attribution 4.0 International License (<https://creativecommons.org/licenses/by/4.0/>), which permits unrestricted use, sharing, adaptation, distribution and reproduction in any medium or format, for any purpose, even commercially, as long as you give appropriate credit to the original author(s) and the source, provide a link to the Creative Commons license, and indicate if changes were made.



capacity of $\sim 7.08 \text{ mA h cm}^{-2}$ under a high sulfur loading of 6.6 mg cm^{-2} . This g-C₃N₄-assisted strategy opens a new gate for the design of an integrated catalysis-conduction network for high-performance LSBs.

Keywords: g-C₃N₄, NbN catalyst domains, conductive network, separator modification, Li-S batteries

INTRODUCTION

The ever-growing demand for energy storage for evolving mobile devices, such as electro-vehicles, pushes the development of energy storage materials. This is due not only to the limited and uneven distribution of fossil energy in different countries and regions but also to the vital commitment to achieving carbon peak and carbon neutrality^[1]. The lithium-sulfur battery (LSB), owing to its satisfying theoretical capacity of $1,672 \text{ mAh g}^{-1}$ and relatively low cost, is becoming a promising candidate in energy storage systems^[2]. However, the intrinsic electron insulativity and self-redox mechanism of the sulfur cathode during the charge/discharge processes would lead to sluggish kinetics and high polarization^[3], as well as the unbearable “shuttle effect”^[4]. The shuttle effect is caused by the dissolution of the lithium polysulfide (LiPS) intermediates in an electrolyte, which decreases the ionic conductivity of the electrolyte and the use of sulfur. The dissolved LiPSs would transfer to the anode side, leading to the self-discharging and fast consumption of active materials.

Plenty of strategies have been applied to ease the aforementioned shortcomings, including cathodic structure design^[5,6] and electrolyte formula modulation^[7,8]. Beyond these, the separator modification also becomes attractive due to its tailored functions to retard the direct contact between the active anode and cathode materials but allow the selective ion transfer^[9,10]. By simply loading the functional coating on the separator at the cathode side, the shuttle effect of LiPSs can be effectively mitigated. In this respect, two main reasons should be considered: (1) The blocking function of modified coating on the relatively large pores of a pristine polypropylene (PP) separator can prevent the straight transfer of large LiPSs molecules; (2) The interaction between polar separator decoration and polar LiPSs through electrostatic adsorption or chemical bonding can also prevent the leakage of LiPSs from the cathode side^[11,12]. Carbon-based materials with controllable morphology were first introduced as separator decorations to improve the electrochemical performance of LSBs^[13,14]. However, even though the transportation behavior of LiPSs at the cathodic side can be modulated by the guidance of channels in carbon materials, the Van der Waals force between the carbon modification layer and LiPSs is not strong enough to capture the LiPSs molecules^[15]. Thereafter, the heteroatom doping (N, O, *etc.*) in carbon materials was proposed to introduce the strong Lewis acid-base interaction between Li⁺ cation in LiPSs and electronegative N or O atoms^[16,17]. In addition, the carbon materials can also be modified by two or more kinds of elements, e.g., in the form of metal alloys^[18], metal oxides^[19], metal sulfides^[15], metal nitrides^[20,21], *etc.* These combinations are flourishing because of the potential synergistic effect between different elements. For example, the Ni/Co/KB (KB: Ketjen black) composite derived from Prussian blue analog was adopted as the modified layer on the separator, where the mesoporous matrix of KB not only promotes the electrolyte penetration but also untangles the polysulfide shuttle effect, and the encapsulated Ni and Co elements in composite do a great favor to the conversion reaction kinetics^[11]. A similar strategy was delivered by adopting nitrogen-doped graphene and two metals into Ni₃Sn₂ alloy^[18]. Unlike the limited element metals doped in the carbon matrix, the non-noble transition metal nitrides (TMNs) are easier to fabricate and exhibit a competing potential because of the low-cost and satisfying electrocatalysis properties^[22]. The combination of metal and nitrogen would narrow the d-band of the metal, delivering the electron structure of TMNs similar to noble metals in the Fermi Level and therefore improving the activity of catalysis sites^[23]. For instance, Zhang *et al.* synthesized a bimetallic nitride of Ni_{0.2}Mo_{0.8}N blended with carbon nanotubes to modify the separator, and it can construct an internal electric field to suppress the shuttle of polysulfides^[22]. The change of electron structure by the Mo

doping makes the corresponding LSBs a better electrode conductivity and catalytic effect on polysulfides.

Based on previous research, niobium nitride possesses a high electron conductivity and high chemical stability against the electrochemical environment^[24]. When embedded in the carbon framework as a sulfur host material, the polar NbN is expected to interact with the free LiPSs in electrolyte and promote the conversion reaction of LiPSs to $\text{Li}_2\text{S}_2/\text{Li}_2\text{S}$ ^[20,21,25]. In order to maximize the catalytic effect of NbN, its contact environment with electronic/ionic conductive substrate and LiPSs is crucial. The aggregation of NbN particles with the loss of electrocatalysis surface or the loose blending of NbN with dense or small-surface carbon materials would seriously degrade the performance of LiPS conversion. However, the uniform and sufficient loading of fine NbN nanoparticles in monolithic porous carbon hosts is still a big challenge. The prior fusion of Nb, N, and C element precursors is highly required to achieve the desired catalyst-in-conductor composite host. Here, we developed a molten salt method to prepare the NbN nanoparticle catalyst evenly loaded in the porous 3D carbon matrix that derives from the g- C_3N_4 precursor. This novel NbN in carbon structure (denoted as NbN/C) is used as a separator modification layer for LSBs with the following merits. First, the synthesis strategy is simple and of one-pot feature. The g- C_3N_4 precursor is chosen as the dual source of the nitridation effect and the remaining carbon skeleton. The resultant modification layer with a 3D porous structure enables the sufficient contact area between the electrolyte and NbN/C composite, beneficial for the LiPSs adsorption, catalysis, and conversion reaction. The corresponding LSBs deliver a highly reversible cycling performance under a high rate of 2 C, with a capacity retention of 72.7% after 1,000 cycles and a satisfying rate performance even under the higher rate of 5 C. When the sulfur loading in the cathode is increased to 6.6 mg cm^{-2} , a high areal capacity of 7.08 mAh cm^{-2} can be realized.

RESULTS AND DISCUSSION

Figure 1A shows the schematic of a one-pot strategy to synthesize a 3D porous carbon skeleton with evenly-embedded NbN nanoparticles. Simply, the precursors of niobium ethoxide and g- C_3N_4 are well mixed in the molten salt of NaCl under the inert atmosphere. In this process, the N element in g- C_3N_4 is extracted by breaking the C-N bond under the potential catalysis effect of thermal Nb cation. The residual C element from the nanosheet self-assembled g- C_3N_4 microsphere is precipitated in the form of a porous and monolithic carbon framework with the preservation of nanosheet structure units. The high inner porosity of this carbon framework and its g- C_3N_4 template precursor is favorable for the injection and diffusion of niobium ethoxide under the molten salt environment, leading to the bonding of released N atoms and injected Nb cations and nucleation of NbN inside the porous framework. The quick inward diffusion of low-boiling-point niobium ethoxide can retard the irregular accumulation of NbN catalyst near the outer surface or even out of the carbon framework. The space confinement in the carbon framework limits the growth of NbN precipitates. Therefore, the NbN nanoparticles located uniformly in the 3D carbon network can be acquired. Such optimization of NbN particle size and distribution is favorable for the performance of LSBs, as discussed later.

The X-ray diffraction (XRD) pattern (as shown in Figure 1B) of the synthesis product fits well with the face-centered cubic NbN phase (JCPDS No. 38-1155) with the characteristic peaks corresponding to (111), (200), (220), and (311) planes. The XRD result with a rare impurity peak indicates the successful production of NbN with good crystallinity. The broad peak located at the smaller angle is ascribed to the carbon species derived from g- C_3N_4 , and it tells the high defect concentration in carbon material that is beneficial for the improvement of conductivity^[26,27]. The NbN phase is expected to deliver a high electron conductivity due to its 0 eV band gap, which is determined by the density functional theory (DFT) calculation (as shown in Figure 1C). Both the high conductivities of the carbon matrix and embedded NbN nanoparticles favor the

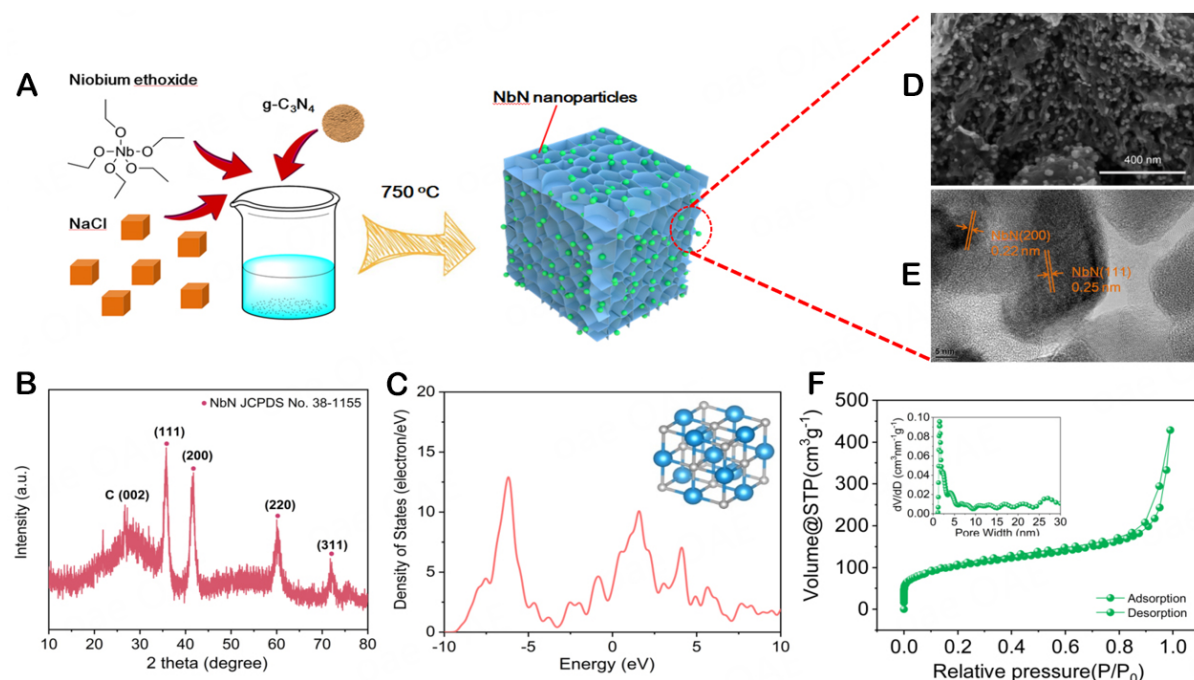


Figure 1. (A) Synthesis process schematic of NbN/C composite. (B) XRD pattern of NbN/C. (C) Band gap of NbN through DFT calculation. (D) SEM image and (E) TEM image of as-synthesized NbN/C. (F) N_2 adsorption-desorption isotherms of NbN/C, inset: pore size distribution based on the BJH method.

kinetics of soluble LiPS conversion into solid Li_2S_2/Li_2S , especially in the contact area between the sulfur cathode and the modified side of the separator. The X-ray photoelectron spectroscopy (XPS) results of the primary NbN/C powder are shown in [Supplementary Figure 1](#). Therein the existence of the strongest C-C peak located at 284.8 eV indicates that most of the three C-N bonds (C-N=C, N-C₃, and C-N-H) in the g-C₃N₄ precursor are broken in the final NbN/C powder. From the residual bonds of C-N=C/N-(C)₃ in N 1s and C-N in C 1s and their intensity comparison, we can deduce the g-C₃N₄ is prone to be scissored from the C-N-H region, then C-N=C region, and finally N-C₃ region during the synthesis. The formation of NbN is further indicated by the appearance of NbN peaks at 397.2 eV in N 1s and 204.0 eV in Nb 3d_{5/2}. The bright spots in the scanning electron microscope (SEM) images (as shown in [Figure 1D](#) and [Supplementary Figure 2](#)) prove the evenly-distributed NbN nanoparticles in the monolithic micro-sized carbon matrix consisting of nanosheet structure units. The residual of C-N=C/N-(C)₃ moieties can help preserve the monolithic carbon framework to some degree, preventing it from fragmentation into the much smaller discrete nanosheet units. These signals also suggest the potential existence of broken C_xN_y in the carbon matrix. From the energy dispersive spectroscopy (EDS) mapping result of the NbN/C powder, the atomic ratio of C/N is nearly 25/2 (as shown in [Supplementary Figure 3](#)). This value is far from the stoichiometry of g-C₃N₄. The loading uniformity and permeability of NbN nanoparticles (with a size around 20 nm) across a thin-layer carbon network is further disclosed by the transmission electron microscope (TEM) observation (as shown in [Supplementary Figure 4](#)). From the high-resolution TEM (HRTEM) imaging, one can observe the lattice fringes corresponding to (200) and (111) planes of cubic NbN (as shown in [Figure 1E](#)), agreeing with the XRD result. The porosity of NbN/C is analyzed by using a nitrogen adsorption-desorption isotherm, as shown in [Figure 1F](#), which delivers a type IV isotherm with a hysteresis loop at high relative pressure and reveals a mesoporous structure in accordance with the aforementioned SEM or TEM studies. The mesopore size distribution is acquired according to the Barrett-Joyer-Halenda (BJH) analysis on the desorption branch of the NbN/C sample (inset of [Figure 1F](#)), indicating the pore size

range is mainly around 2.2-5 nm. The narrow pores left after N extraction from the nanosheet structure units are responsible for such a pore size distribution. The specific area is calculated to be as high as $335.4 \text{ m}^2 \text{ g}^{-1}$ by the Brunauer-Emmett-Teller (BET) method, which is much higher than that ($88.5 \text{ m}^2 \text{ g}^{-1}$) of the $g\text{-C}_3\text{N}_4$ precursor as reported in our previous work^[28,29]. The increase of specific surface area further confirms the extra pore creation by the N extraction from $g\text{-C}_3\text{N}_4$, as well as by the pillaring of NbN nanoparticles between carbon layers. The planting of NbN nanoparticles can effectively expand the carbon framework and retard its structure collapse during cycling. This configuration would favor the electrolyte penetration and enlarge the reaction area of LiPS conversion.

The mesoporous structure and polar NbN bonding in NbN/C composite are expected to be favorable for the fast penetration of electrolytes. The electrolyte wettability of PP separators with and without NbN/C decoration was measured by contact angle experiments. As shown in [Figure 2A](#), the modified PP delivers a much smaller contact angle of only 3.6° , which is much lower than that of the blank PP (46.9° , detected in the same condition). Besides, the digital images of fold tests of the modified separator in [Figure 2B](#) tells the high adhesion of the NbN/C layer on PP, and there is no peel-off phenomenon of attached substance or cracking phenomenon even after folding the modified separator several times. The porous surface of the carbon skeleton and the vacuum filtration process greatly benefit the combination between NbN/C and PP substrate by not only enlarging the contact area but also providing air pressure to condense the NbN/C layer. To compare the surface morphologies of the separators before and after modification, the corresponding SEM images are shown in [Figure 2C](#) and [D](#). The blank PP shows a flat surface with plenty of open porous tunnels (as shown in the inset of [Figure 2C](#)) that are beneficial for ion and mass transportation. On the contrary, the NbN/C decorated separator (denoted as NbN/C@PP) exhibits a scratchy structure with hierarchical porosity, which still allows the facile wetting of electrolytes. The thickness of the modifier layer in [Figure 2E](#) is measured to be about $8.07 \mu\text{m}$. In the modifier layer, both the carbon skeleton and NbN can physically and chemically absorb the dissolved LiPSs, preventing them from arriving at and passing across the PP separator^[30]. The metal nitride can even further catalyze the conversion reactions of LiPS intermediate products to the final solid products of $\text{Li}_2\text{S}_2/\text{Li}_2\text{S}$, as discussed later, further mitigating the shuttling of dissolved LiPSs across the separator.

As shown in [Figure 2F](#), the dissolution of Li_2S_4 in the tetraethylene glycol dimethyl ether (TEGDME) makes it turn from a colorless solvent into a yellow solution. When carbon black is added into the Li_2S_4 solution with vigorous stirring and then standing for 72 h, the solution still remains yellow, indicating the weak adsorption effect of pure carbon on LiPSs. In contrast, the color of the solution after adding NbN/C changes back and becomes colorless, suggesting the strong adsorption ability of NbN towards LiPSs. To further prove the adsorption effect, DFT calculation was applied to calculate the adsorption energies between Li_2S_4 and different additives. As shown in [Figure 2G](#), the adsorption energy between Li_2S_4 and carbon black is -0.13 eV , which is not strong enough for carbon black to capture Li_2S_4 . However, the adsorption ability of NbN/C is much stronger in view of the much more negative bonding energy of -2.09 eV due to the potential bonding of Li-N and S-Nb. The calculation result corresponds to the above visualization experiment. When the NbN/C composite is applied as the modifying layer on the separator, the “shuttle effect” is greatly inhibited, as shown in [Figure 2H](#). The H-type container used here is composed of two small bottles that are separated by different separators. The bottle on the left is filled with the electrolyte with dissolved LiPSs, while the one on the right is filled with pure electrolytes. Two different separators of blank PP and NbN/C@PP are applied to investigate the restriction function of NbN/C on the transference of LiPSs. After standing for 1 h, a certain amount of LiPSs has been transported through the blank PP, and the electrolyte on the right becomes yellow. When the staying time is extended to 6 h, a much more severe “shuttle effect” of LiPSs happens with the appearance of more LiPSs in the right electrolyte. On the contrary, the

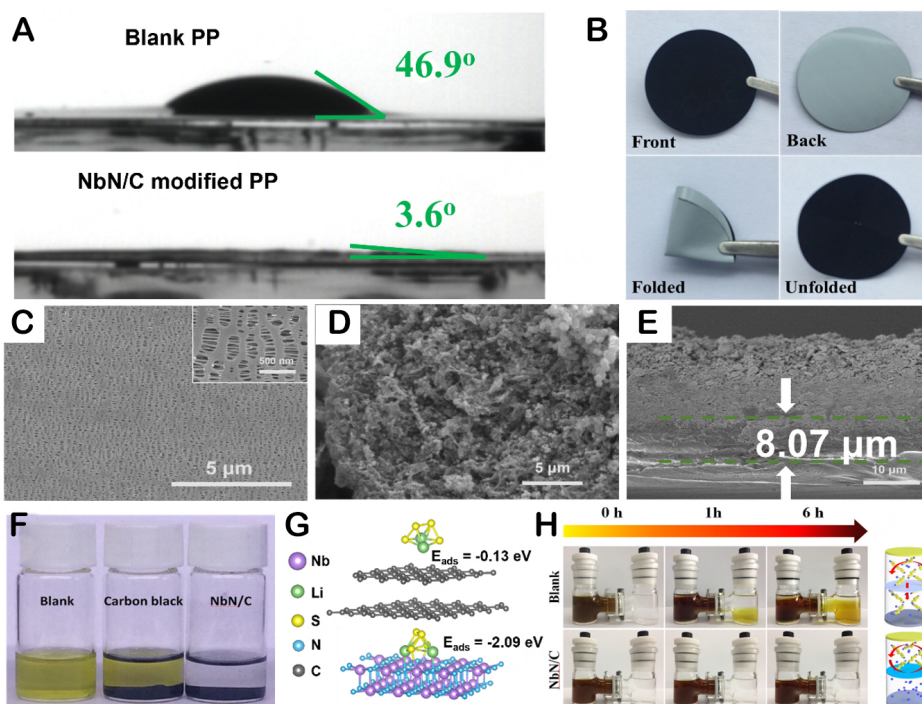


Figure 2. (A) Contact angle test on NbN/C-modified PP (bottom) and pristine PP (upper). (B) Folding test to prove the strong adhesion of the modifying layer to PP. SEM images of (C) pristine PP separator and NbN/C@PP from (D) top view and (E) cross-section view. (F) Digital images of adsorption test in Li_2S_4 solutions before and after adding carbon black and NbN/C. (G) Adsorption energy calculation of Li_2S_4 on the surfaces of C (upper) and NbN (200) (bottom). (H) “Shuttle effect” test by using an H-type container with different separators: NbN/C@PP (bottom) and pristine PP (upper).

NbN/C@PP enables the different electrolytes at both sides to keep their initial states no matter the standing time changes. This is because the NbN/C on the left side of the PP separator stops the transference of LiPSs, as illustrated in the schematics. The strong adsorption ability of NbN towards LiPSs and the hierarchical mesoporous feature of stacked carbon layers are responsible for the above phenomena.

As shown in Figure 3A, the shuttle current was measured, and it derives from the self-discharge, i.e., the shuttle effect. By holding the Li-S cell with NbN/C@PP or blank PP separator under a voltage of 2.38 V for a long time, an obvious disparity for the two cells on the shuttle current is presented. The shuttle current for the NbN/C@PP-based cell is around $2.39 \times 10^{-3} \text{ mA cm}^{-2}$, which is much lower than that for blank PP ($29.18 \times 10^{-3} \text{ mA cm}^{-2}$). This disparity further proves the existence of strong and abundant adsorption sites on the NbN/C@PP separator, thereby greatly restricting LiPSs and suppressing the “shuttle effect” in the Li-S cell. It is worth noting that the galvanostatic (dis)charge is a dynamic process during which the charge transfer would have a great impact on the electrochemical performance, such as voltage hysteresis, electrochemical resistance, and more^[31]. Hence, besides the function of adsorbing LiPSs, a higher demand for accelerating polysulfide conversion in the modifying layer is required. The NbN/C layer, as expected, shows a satisfying catalytic property on the LiPS conversion reactions, as illustrated by kinetics analysis. The redox reaction between S_8 and Li_2S on NbN/C and blank carbon are compared by using cyclic voltammetry (CV) in symmetric cells at 1.0 mV s^{-1} , which have the identical working and counter electrodes, and 1 M lithium bis(trifluoromethanesulfonyl)imide (LiTFSI) solution with 0.1 M Li_2S_6 is used as an electrolyte. Two pairs of symmetric redox peaks are clearly exhibited for NbN/C electrodes in Figure 3B, whereas the redox peaks for blank carbon electrodes are less symmetric with more redox stages. The former peaks are much sharper and have smaller voltage hysteresis than those for the latter, indicating the faster liquid-solid

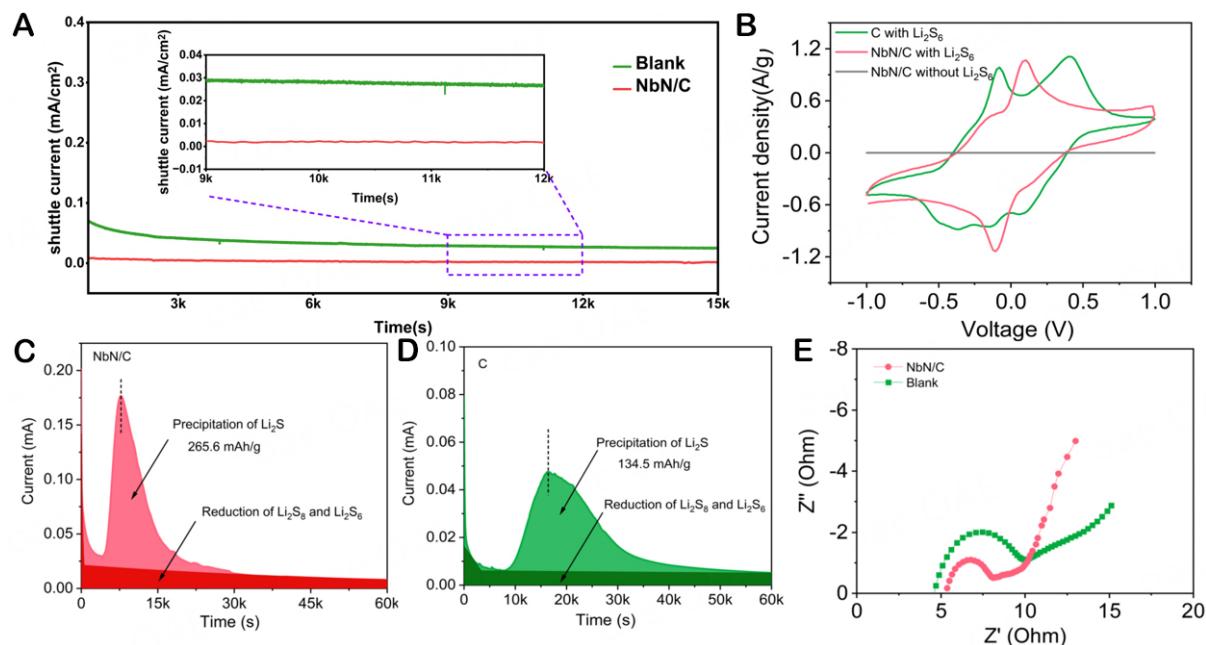


Figure 3. (A) Shuttle current comparison of Li-S cells by using different separators. (B) CV curves of Li|Li symmetric cells with/without 0.1 M Li_2S_6 . Current vs. time curves with different stages of reductions of Li_2S_8 and Li_2S_6 and precipitation of Li_2S during potentiostatic discharge of Li_2S_8 /TEGDME catholyte by using (C) NbN/C@PP and (D) PP separator at 2.05 V. (E) EIS result of Li-S cells discharged to 2.05 V with different separators.

conversion reactions associated with Li_2S_6 adsorbed by NbN/C. There is no redox peak observed for the NbN/C electrode when the Li_2S_6 -free electrolyte is used. Note that a new pair of peaks (a/a') emerge under the relatively higher scan rates in the case of NbN/C (as shown in [Supplementary Figure 5](#)). The appearance of this couple of peaks with larger voltage polarization indicates the longer survival time of the shorter-chain polysulfide anion (S_4^{2-}) due to the catalysis effect of NbN^[5]. Because the Li_2S precipitation from Li_2S_4 intermediate conversion shares three-quarters of the whole theoretical capacity during the discharge process of sulfur^[32], the electrodeposition rate of Li_2S on the substrate material could be an important kinetics indicator for LSBs. Here, the potentiostatic discharge curves of two coin cells with different separators at 2.05 V are compared, as shown in [Figure 3C](#) and [D](#). To mitigate the influence of long-chain polysulfides, the cells are firstly discharged to 2.06 V, and then a small bias of 0.01 V is applied to drive the nucleation and growth of Li_2S ^[33]. According to the research of Lu^[34], the Li_2S deposition complies closely with the 2D instantaneous nucleation model in a glyme-based electrolyte, and the relationship between reaction time (t) and current response (J) can be quantitatively modeled through the following equation^[35]:

$$\frac{J}{J_m} = \left(\frac{t}{t_m}\right) \exp\left[-\frac{1}{2}\left(\frac{t^2}{t_m^2} - 1\right)\right]$$

where J_m and t_m represent the peak current and the time when the peak current occurs, respectively. Obviously, the cell with an NbN/C-modified layer shows a higher current peak at the earlier time compared with the case of bank carbon. The much sharper peak indicates that the high-density NbN domains in the system can greatly improve the conversion reaction of Li_2S_4 into Li_2S . The capacities of Li_2S precipitation calculated from the integral of current vs. time are 265.5 mAh g^{-1} and 134.5 mAh g^{-1} for the separator-modified and unmodified cells, respectively. The rate of Li_2S electrodeposition during the potentiostatic process can be calculated using the following equation:

$$t_m = (2\pi N_0 k^2)^{-0.5}$$

in which N_0 represents the areal density of Li_2S nuclei, and $N_0 k^2$ gives the effective rate constant for the Li_2S coverage on the electrode surface^[35]. The $N_0 k^2$ value is $2.62 \times 10^{-9} \text{ s}^{-2}$ for NbN, much higher than that of the control cell ($5.92 \times 10^{-10} \text{ s}^{-2}$). This analysis indicates that the thin-layer carbon matrix loaded with high-density NbN nanodomains can provide sufficient nucleation sites for Li_2S due not only to the sulfiphilic property of metal nitride surface but also to the potential catalysis function as discussed later with DFT calculation.

The electrochemical impedance spectra (EIS) of corresponding cells were also measured. When both the cells are discharged to 2.05 V, the impedance of the NbN/C-based cell shows a much smaller semicircle and a steeper slope at the low-frequency region (as shown in [Figure 3E](#)) compared with the case of the control cell, proving the faster charge transfer and Li diffusion at the stage of reduction to solid $\text{Li}_2\text{S}_2/\text{Li}_2\text{S}$ under the help of the NbN catalyst^[36]. To better understand the conversion reaction of the sulfur cathode under different separators, the CV test on the Li-S cells was conducted at a scan rate of 0.2 mV s^{-1} , as shown in [Figure 4A](#). Two cathodic peaks can be detected for both the cells and taking the NbN/C case as an example, the higher peak at 2.35 V corresponds to the reduction process of S_8^{2-} and S_6^{2-} polysulfides to S_4^{2-} and the other peak at 2.03 V represents the nucleation of solid $\text{Li}_2\text{S}_2/\text{Li}_2\text{S}$ by the deeper reduction from Li_2S_4 . Both the higher voltage of long-chain polysulfide reduction and the stronger current response of $\text{Li}_2\text{S}_2/\text{Li}_2\text{S}$ precipitation under the assistance of NbN/C indicate the improved kinetics of multi-step conversion reactions. The advantage of reconversion reaction kinetics is also observed for the NbN/C case in view of the larger area of anodic peak current response. The Li diffusion coefficient D_{Li^+} as another kinetics indicator can be acquired by introducing the CV curves at different scan rates from 0.1 to 0.4 mV s^{-1} (as shown in [Supplementary Figure 6](#)). According to the linear relationship between peak current density (I_{pa}) and the square root of scan rate (ν), the D_{Li^+} value can be obtained according to the Randles-Sevcik equation^[37]:

$$I_{pa} = 268600 n^{1.5} A D_{\text{Li}^+}^{0.5} C \nu^{0.5}$$

Here, n is the number of reaction electrons (e.g., for the second cathodic process investigated, $n = 2$), A is the area of the cathode (0.785 cm^2), and C represents the concentration of Li^+ in the electrolyte ($0.0012 \text{ mol cm}^{-3}$). As shown in [Figure 4B](#), the existence of NbN/C on the separator improves the Li diffusion coefficient from $3.633 \times 10^{-8} \text{ cm}^2 \text{ s}^{-1}$ to $1.748 \times 10^{-7} \text{ cm}^2 \text{ s}^{-1}$. The kinetic optimization is also reflected in the galvanostatic curves during charge and discharge processes (as shown in [Figure 4C](#)). As seen, the voltage hysteresis (169 mV) for the NbN/C-modified Li-S cell is smaller than that (192 mV) of the control cell. Besides, there are two obvious nucleation overpotentials at the liquid-solid and solid-liquid conversion stages during the cycling of Li-S cells without NbN/C decoration. However, these bulge points nearly disappear after the introduction of NbN/C, suggesting the potential catalysis of high-density NbN domains in these relatively sluggish conversion stages. This phenomenon is also consistent with the faster charge exchange as obtained by Tafel plots. Specifically, a voltage range of $\pm 200 \text{ mV}$ is applied to the coin cells with different separators at the specific voltages, which are determined by the reduction and oxidation peak positions in the CV test. As expected, the NbN/C-modified cell displays a lower Tafel slope of 126 mV dec^{-1} at the stage of S_8 -to- Li_2S_n conversion and 56 mV dec^{-1} at the stage of Li_2S_n -to- Li_2S conversion when compared with those of the control cell (as shown in [Figure 4D](#) and [E](#)). When the cells are recharged, the lower Tafel slope of 55 mV dec^{-1} for Li_2S -to- Li_2S_n is also detected for the modified cell (as shown in [Supplementary Figure 7](#)). These results further confirm the accelerated liquid-to-solid and solid-to-liquid conversions, benefiting from the catalysis of NbN domains. Based on the Tafel slopes, the difference in

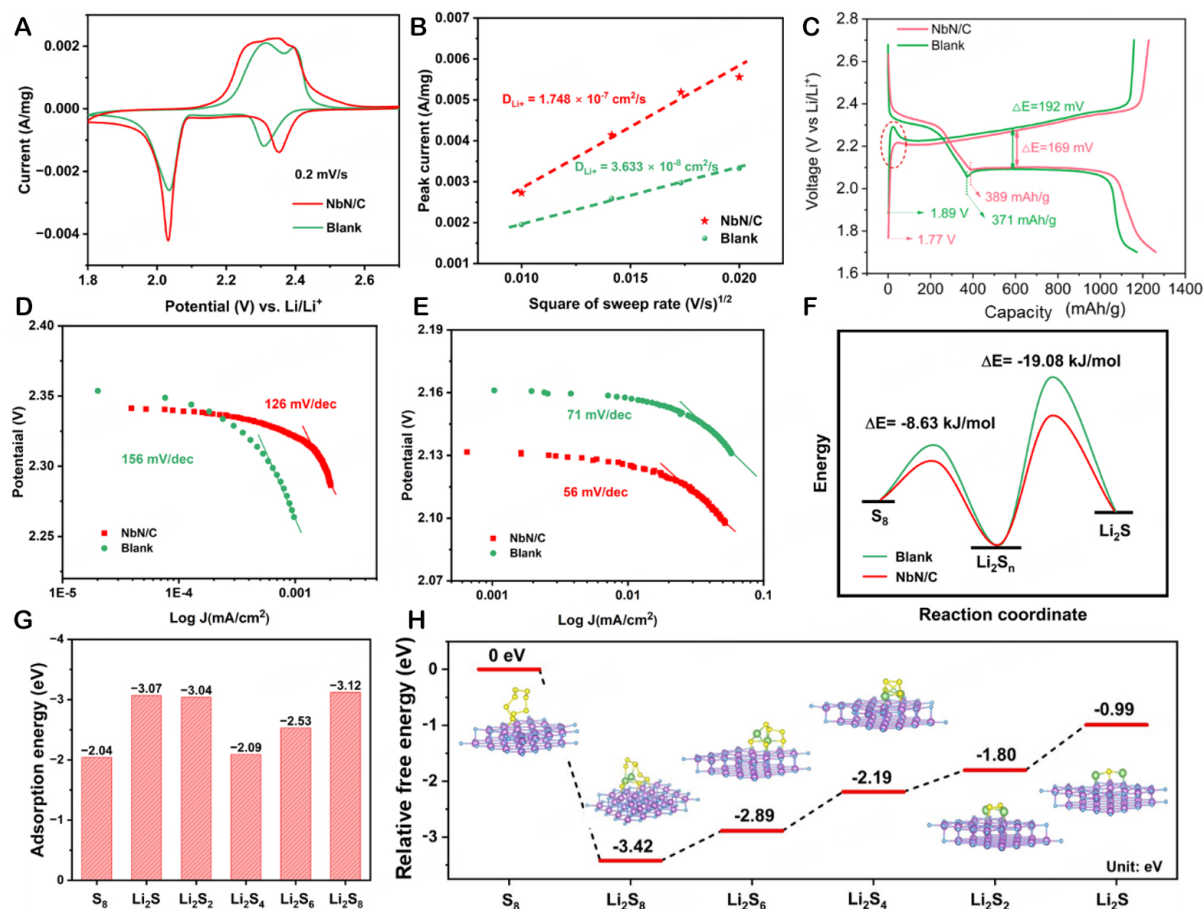


Figure 4. (A) The CV test on the Li-S cells using different separators under a scan rate of 0.2 mV s^{-1} . (B) Diffusion coefficient calculation based on the relationship of peak current and square of sweep rate from CV profiles at different sweep rates. (C) Galvanostatic discharge and charge curves under a rate of 0.2 C . Tafel plots corresponding to the reduction reactions (D) from elemental sulfur to Li_2S_n and (E) from Li_2S_n to Li_2S . (F) Relative activation energy evolution of S_8 - Li_2S_n - Li_2S conversion reactions based on different separators. (G) Adsorption energies and (H) Gibbs free energy profiles of LiPSs on the surface of NbN (200) by DFT method.

activation energies (E_a) for corresponding conversion stages can be calculated^[38]. The detailed information is listed in Note S1 in Supporting Information, and the result is summarized in Figure 4F. Both the activation energies for the reduction processes of S_8 -to- Li_2S_n and Li_2S_n -to- Li_2S are obviously decreased by 8.63 kJ mol^{-1} and $19.08 \text{ kJ mol}^{-1}$, respectively, after the introduction of NbN/C, strongly supporting the proposed catalyst ability of NbN/C on the separator. Therefore, the sluggish conversion reactions caused by the substantial phase changes are greatly activated.

To better understand the function of NbN on the conversion reaction of LiPSs, DFT calculation is further applied. The adsorption energies of different LiPSs on the (200) plane of NbN are summarized in the column graph in Figure 4G, and they are all higher than 2 eV (as shown in Supplementary Table 1). The high adsorption energies would greatly help the NbN on PP to catch the dissolved LiPSs in the electrolyte during cycling and inhibit their shuttle effect. It is worth noting that both the Li and S in the polysulfides show an interconnection with the NbN surface (the schematics of corresponding adsorption systems are inserted in Figure 4H), and some broken S-S bonds within long-chain LiPSs indicate the catalytic function of NbN with the acceleration of conversion reaction. This is in accordance with the small overpotential observed in CV curves and in the electrochemical cycling tests. Besides, the Gibbs free energies (ΔG) of the

main intermediates from S_8 to Li_2S under the catalysis of NbN are calculated, and ΔG is an effective indicator to investigate the conversion mechanism, as listed in [Figure 4H](#). Taking the system of S_8 with NbN as the reference, the first step of S_8 transformation into Li_2S_8 is a spontaneous exothermic reaction with the decrease of relative free energy of -3.42 eV. The following four steps, on the contrary, are all endothermic reactions, showing a growing ΔG from Li_2S_8 to Li_2S , and the corresponding energy barrier value for each conversion step is listed in [Supplementary Table 2](#). Even so, the whole energy from S_8 /NbN to Li_2S /NbN system is decreased under the catalysis of NbN. Note that the conversion step from Li_2S_2 to Li_2S requires overcoming the highest energy barrier of 0.81 eV, making it the rate-controlling step during the discharge process^[39].

The electrochemical performance of LSBs was measured under a high rate of 2 C (1 C = 1,672 mA g⁻¹) within the voltage range of 1.7-2.8 V. [Figure 5A](#) displays the long cycling performance of LSBs with/without the NbN/C-modified PP separator. Under the strong adsorption and catalysis effects of NbN, the modified cell has a much higher specific capacity and a more stable capacity retention of 72.7% (from 771.8 to 561.1 mAh g⁻¹) than that of the control cell (47.4%) even after 1,000 cycles. Due to the poor conductivity and volume change of sulfur cathode during cycling, the cathode and modification coating may be passivated or deformed, and it would lead to degradation of the use of active materials, especially after long-term cycling. Besides, the roughening of the Li metal anode during long-term cycling would consume the electrolyte and cause capacity degradation. Note that the specific capacity of cells using Al foil as current collectors decreases faster than that using carbon paper, although they exhibit a similar performance during the first 200 cycles (as shown in [Supplementary Figure 8](#)). The main reason for this phenomenon could be ascribed to the easier exfoliation of S-based active material from the relatively smoother Al foil than from the relatively rougher carbon paper during cycling, in view of the volume change during the S-based conversion reaction. The activated kinetics of the LiPS conversion reaction should be ascribed to the addition of NbN, and it is also reflected in the charge/discharge curves (as shown in [Figure 4C](#)). The rate performance of the modified cell is also improved with the current density changing from 0.2 C to 5.0 C (with reversible capacities of 742.6, 696.6, and 652.6 mAh g⁻¹ at 3, 4, and 5 C, as shown in [Figure 5B](#)), and the reversible capacity would return back immediately once the rate is back to 0.2 C, indicating good structure stability of NbN/C network during high-rate cycling. When the sulfur loading is increased to as high as 6.6 mg cm⁻², the NbN-modified cell still exhibits stable cycling for more than 100 cycles under the current density of 1 mA cm⁻² and electrolyte-to-sulfur ratio (E/S ratio) of 5 μ L/mg, as shown in [Figure 5C](#) and [Supplementary Table 3](#). Under the lean electrolyte condition, the areal capacity reaches approximately 7.08 mAh cm⁻² after a prior activation process of 2 cycles and is preserved at 5.61 mAh cm⁻² (850 mAh/g) after 100 cycles. This performance is relatively satisfying when compared with some others reported before, as listed in [Supplementary Table 4](#). We also tested the Li-S cells with different loadings of cathodes (as shown in [Supplementary Figure 9](#)). Although the capacity of the cell with 6.6 mg cm⁻² loading decays after 100 cycles, the discharge capacity is still much higher than that in the case of 7.8 mg cm⁻² loading and is close to the case of 3.4 mg cm⁻² loading.

The cycled Li-S cell with a modified PP separator was disassembled to investigate the chemical information on the surface of NbN/C (e.g., the interaction situation of NbN with LiPSs) by XPS method (as shown in [Figure 5D](#) and [E](#), and [Supplementary Figure 10](#)). Note that the Nb 3d region has a splitting of spin-orbit components with a distance of 2.78 eV between Nb 3d_{3/2} and 3d_{5/2} peaks. The peak splitting distance for S 2p is 1.16 eV between S 2p_{1/2} and 2p_{3/2}. The NbN peak is found at 204.5 eV in Nb 3d_{5/2}^[25]. The peaks of Nb-O/NbN-O (at 207.0 and 205.5 eV, respectively) could also be detected in view of the potential reaction between NbN and electrolyte during cycling and the potential O dopant transfer from O-doped g-C₃N₄ into NbN. The trapping of LiPSs (and even Li_2S_2 / Li_2S) and their shuttle suppression by NbN/C are indicated from the

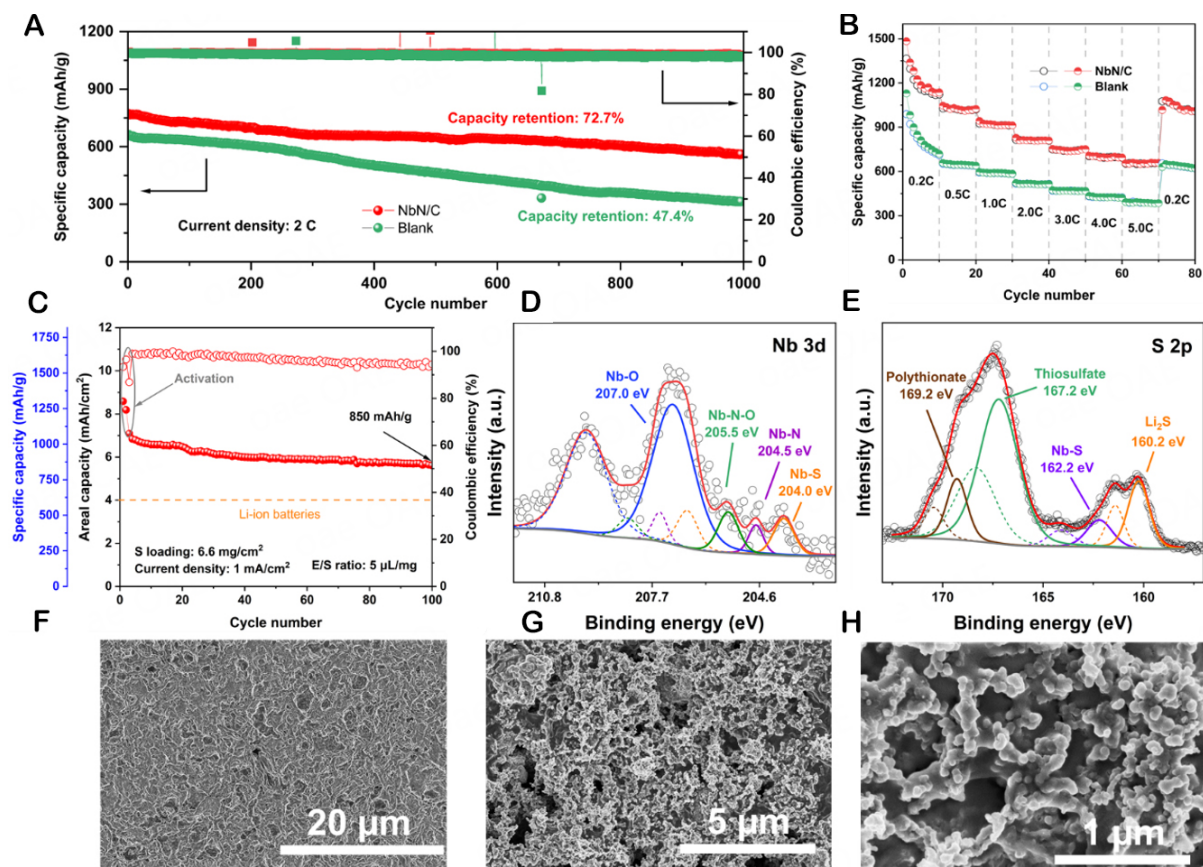


Figure 5. (A) Cycling stability test of Li-S cells based on different separators at a rate of 2 C. (B) Rate performance of Li-S cells at different rates from 0.2 C to 5.0 C. (C) Cycling performance of Li-S cell using NbN/C@PP as separator with a high sulfur loading of 6.6 mg cm^{-2} under a current density of 1 mA cm^{-2} . XPS spectra of the surface of cycled NbN/C@PP separator in (D) NbN 3d and (E) S 2p. SEM images of (F) lithium anode and (G and H) NbN/C@PP separator after cycling for 50 cycles.

appearance of Nb-S peaks at 204.0 eV and 162.2 eV as observed in Nb $3d_{5/2}$ and S $2p_{3/2}$, respectively^[25]. The interaction between Nb cation- and S-based species is in accordance with the DFT calculation results. Note that there are no substantial peaks of long-chain polysulfides in S 2p, but the Li_2S signal (160.2 eV) at the discharged state indicates the thorough conversion of LiPSs to Li_2S under the catalyst of NbN^[40,41]. There are also the peaks corresponding to the thiosulfate and polythionate species detected at 167.2 and 169.2 eV in S $2p_{3/2}$, respectively^[24]. The thiosulfate should be the result of the redox reaction between LiPSs and modifying layer on PP, and the subsequent reaction of thiosulfate with LiPSs is responsible for the formation of polythionate. The morphologies of the lithium metal anode and NbN/C-modified layer near the cathode side after 50 cycles are observed by SEM imaging. The cycled Li metal surface is still flat without evident dendrite growth but with some pits (left after Li stripping), as shown in Figure 5F. As shown in Figure 5G, the cycled NbN/C layer does not collapse or agglomerate under the galvanostatic process, and it still holds a similar porous morphology as the original structure. The interconnected carbon skeleton derived from C_3N_4 is well preserved and is still loaded with sufficient and dispersed NbN nanoparticles (as shown in Figure 5H). These features do not degrade the electrolyte wettability at the cathode side, enabling the enlarged contact of LiPSs with the NbN/C interlayer. The large contact area avoids the possible stacking of solid $\text{Li}_2\text{S}_2/\text{Li}_2\text{S}$ precipitates (as shown in Figure 5H), and the high dispersity of conversion products makes them possible for a sustainable reaction during long-term cycling.

CONCLUSION

In summary, we propose to scissor the g-C₃N₄ precursor for high-density loading of catalyst domains in mesoporous thin-layer conductive networks via a facile molten salt synthesis method for durable Li-S batteries. The resultant NbN in carbon composite is used as a separator modifier for the strong adsorption towards dissolvable long-chain polysulfide intermediates and their catalytic conversion reactions. The LSBs with the NbN/C@PP separator demonstrate superior long cycling stability (at least 1,000 cycles at a high rate of 2 C) and rate performance (652.6 mAh g⁻¹ at a higher rate of 5 C). The durable cycling is still achievable when the sulfur loading is as high as 6.6 mg cm⁻², delivering a high areal capacity of 5.61 mA h cm⁻² after 100 cycles. This g-C₃N₄-assisted strategy opens a new gate for the integrated catalysis-conduction network for high-performance LSBs.

EXPERIMENTAL SECTION

Material synthesis

Synthesis of g-C₃N₄: The synthesis of the g-C₃N₄ microsphere precursor is based on our previous work^[26]. Specifically, 80 mL melamine (25 g L⁻¹, Alfa Aesar, 99%) and 40 mL cyanuric acid (51 g L⁻¹, CA, Alfa Aesar, 99%) were acquired by dissolving the respective materials into dimethyl sulfoxide (DMSO) under vigorous blending. Then, both solutions were mixed with continuous stirring for 30 min, and vacuum filtration was applied to acquire the white powder. Ethanol was used to remove the residual precursors in the mixture. After drying in the vacuum oven under 80 °C for 12 h, the powder was transferred into a tube furnace for heat treatment under N₂ flow with a heating rate of 3 °C min⁻¹, and the heating process was kept for 4 h at 550 °C to get the pale-yellow g-C₃N₄ microspheres.

Synthesis of NbN/C: A molten salt method was applied to get the NbN/C product in a single step. Specifically, 100 mg niobium ethoxide (Aladdin, 99.95% metals basis), 200 mg g-C₃N₄, and 5 g NaCl were blended uniformly in a mortar, and the mixture was then transferred into a quartz boat for heat treatment under Ar atmosphere at 750 °C for 5 h under a heating rate of 3 °C min⁻¹. Ethanol was adopted to wash the product to eliminate the possible residual precursors. After drying under 80 °C for 12 h, the final NbN/C powder was collected for future use.

Material characterization

Structure investigation: X-ray powder diffractometer (XRD, Bruker, D8 Discover) using Cu-K α radiation was applied to investigate the powder structure within a 2θ range of 10° to 80°. The morphology of NbN/C powder was investigated using scanning electron microscopy (SEM, Magellan 400L, FEI) and transmission electron microscopy (TEM, JEOL JSM-6700F, operated at 200 kV). For the observation of morphologies of the cycled lithium anode and the NbN/C@PP separator, the cell was disassembled after cycling for 50 cycles under a current density of 1 C. Nitrogen adsorption/desorption isotherms were acquired by a Quantachrome Autosorb iQ gas sorption analyzer, and the specific surface area was determined by the BET method. The contact angle test for the electrolyte drops on blank and NbN/C-modified PP was carried out using a contact angle measuring instrument SDC200. The X-ray photoelectron spectroscopy (XPS) result of LiPS adsorption on the NbN/C matrix was measured using an ESCALAB-250 XPS spectrometer equipped with an Al K α source (1,486.6 eV).

Electrochemical measurement: Before the assembly of cells, the modified separator NbN/C@PP should be obtained. Firstly, the as-prepared NbN/C was dispersed into ethanol until a sol was acquired. A 20 wt% polyvinylidene difluoride (PVDF) was added to improve the adhesion ability of the decoration powder on the separator. Then, vacuum filtration was applied to load the NbN/C layer onto one side of the separator (Celgard 3501). By controlling the concentration of the NbN/C sol, the mass loading of the modified

separator can be adjusted. The separator was further punched into discs with a diameter of 19 mm after drying and was then transferred into the Ar-filled glovebox with water and oxygen contents less than 0.05 ppm. To assemble the cells for electrochemical measurement, lithium metal, NbN/C@PP, and S/C were used as the anode, separator, and cathode, respectively. The S/C cathode was prepared by mixing sulfur (S) with Ketjen Black (KB) with S content of 70 wt%. After further mixing of S/C with PVDF at a weight ratio of 9:1, the S/C@PVDF slurry was spread onto the carbon paper to obtain the working electrode. The prepared electrode was placed in a vacuum oven under 60 °C for 12 h. The S-mass loading of the electrode is $\sim 1 \text{ mg cm}^{-2}$ unless specifically labeled. The commonly used Li-S electrolyte (i.e., 1 M LiTFSI salt and 0.2 M LiNO_3 additive dissolved in 1,3-dioxolane and dimethoxyethane DOL/DME, v/v = 1:1, Sigma) was adopted. The galvanostatic tests were conducted under a voltage window of 1.8-2.8 V on LAND-CT2001A. Electrochemical impedance spectra (EIS) measurements were conducted in a frequency range from 1 MHz to 0.1 Hz, with a bias voltage of 10 mV on VersaSTAT3 (AMETEK Science Instruments). Cyclic voltammetry (CV) was adopted to measure the cell kinetics on an electrochemical workstation (VersaSTAT3). For the Tafel tests, the Li-S cells with different separators were first reduced to the voltage that was determined through the CV test, at which the phase charge starts. Taking the NbN/C-modified cell as an example, the cell was first discharged to 2.28 V at a scan rate of 0.3 mV s^{-1} , and then a potentiostatic process was applied for 1 h, followed by the Tafel test within $\pm 200 \text{ mV}$ to obtain the relationship between current and voltage. Three stages corresponding to S_8 -to- Li_2S_n , Li_2S_n -to- Li_2S , and Li_2S -to- Li_2S_n were analyzed.

Li₂S nucleation experiment: To better analyze the nucleation process of LiPSs on NbN/C, the Li-Li₂S₈ system was assembled. Specifically, 0.25 M Li₂S₈ solution in 1 M LiTFSI (dissolved in tetraethylene glycol dimethyl ether TEGDME, G4, Sigma) solution was prepared by mixing S and Li₂S at a molar ratio of 7:1. The solution with 2 wt% LiNO_3 to replace Li₂S₈ was used as the blank electrolyte. NbN/C was mixed with PVDF (9:1) and was then cast onto the carbon paper to acquire the working electrode, and the lithium metal was used as the counter electrode with Celgard 3501 as the separator. Then, 20 μL of Li₂S₈ catholyte and the same volume of the blank electrolyte were dropped onto the working electrode and the counter electrode, respectively, followed by discharging galvanostatically to 2.06 V at 0.112 mA and then standing potentiostatically at 2.05 V for 60,000 s. The rate of Li₂S nucleation on the electrode was calculated based on Faraday's law.

Visualized adsorption and shuttle effect measurements of LiPSs: To examine the adsorption ability of NbN/C on LiPSs, a certain amount (10 mg) of as-prepared NbN/C or carbon black was added into the Li₂S₄ solution (0.5 mmol L^{-1}), which was obtained by dissolving Li₂S and sulfur in TEGDME at a molar ratio of 1:3 during stirring for 72 h. The shuttle prohibition effect of the separator was observed by using an H-type container. The brownish-red Li₂S₆ solution and transparent DOL/DME solution were separated on both sides of the H-type container based on the modified or control separator. The LiPSs diffusion through the separator can be visualized directly.

Shuttle current measurement: The Li-S cells with different separators were first charged and discharged three times at a rate of 0.5 C to reach a relatively stable state. Then the cells were discharged to 2.38 V and switched to the potentiostatic mode to observe the shuttle current on the PARSTAT multichannel electrochemical workstation.

Computational methods

Density functional theory (DFT) calculations were conducted by using the Vienna ab initio simulation package (VASP) within the projector augmented wave (PAW) method^[39,42]. The generalized gradient approximation with the Perdew-Burke-Ernzerh (GGA-PBE) was also carried out to describe the electron exchange-correlation interaction. An energy cutoff of 450 eV and k-points of $3 \times 3 \times 1$ grids were adopted

for the geometric optimization of NbN. The (200) plane of NbN was chosen as the adsorption surface towards LiPSs, and the vacuum layer of the supercell slab is set as 20 Å to avoid the possible interaction between the NbN (200) plane and its periodic layer. The geometric optimizations of Li_2S_n and S_8 molecules were also applied with a $20 \times 21 \times 22 \text{ \AA}^3$ unit cell and a gamma-centered k-mesh ($1 \times 1 \times 1$). For a better description of the interaction within the systems of NbN/ Li_2S_n (S_8), the atoms of NbN were fixed except for the surface layer to get the adsorption energy between the two materials. The DFT-D3 correction method of Grimme was employed for the calculation of the van der Waals interaction between NbN and LiPSs. The energy convergence criterion and the force convergence criteria were set as 10^{-5} eV and 0.03 eV \AA^{-1} , respectively. The adsorption energy (E_{ads}) between the NbN and different LiPSs was obtained through the equation $E_{\text{ads}} = E(\text{S}_8/\text{Li}_2\text{S}_n) + E(\text{NbN}(200)) - E(\text{S}_8/\text{Li}_2\text{S}_n + \text{NbN}(200))$. Here, $E(\text{S}_8/\text{Li}_2\text{S}_n)$, $E(\text{NbN}(200))$ and $E(\text{S}_8/\text{Li}_2\text{S}_n + \text{NbN}(200))$ represent the energies of S_8 or Li_2S_n monomer molecule, $E(\text{NbN}(200))$ slab and the whole system after geometry optimization, respectively. To calculate the free energy of each NbN- Li_2S_n system, the equation $G = E + E_{\text{ZPE}} - TS$ was applied, where G , E , E_{ZPE} , and TS are the free energy, total energy from DFT calculation, zero-point energy, and entropic contribution, respectively.

DECLARATIONS

Acknowledgments

We appreciate the support from the Program of Shanghai Academic Research Leader (21XD1424400).

Authors' contributions

Investigation, Formal analysis, Methodology, and Writing-original draft: Lai C

Investigation, Formal analysis, and Methodology: Zhou X

Investigation and Calculation: Lei M

Investigation: Liu W

Writing-review & editing: Mu X

Conceptualization, Supervision, Methodology, and Writing-review & editing: Li C

Availability of data and materials

Data and materials will be made available on request. All materials and preparation details are shown in the [Supplementary Material](#).

Financial support and sponsorship

This work was financially supported by the National Natural Science Foundation of China (21975276) and Shanghai Science and Technology Committee (20520710800).

Conflicts of interest

All authors declared that there are no conflicts of interest.

Ethical approval and consent to participate

Not applicable.

Consent for publication

Not applicable.

Copyright

© The Author(s) 2023.

REFERENCES

1. Zhang S, Chen W. Assessing the energy transition in China towards carbon neutrality with a probabilistic framework. *Nat Commun* 2022;13:87. DOI PubMed PMC
2. Feng J, Li J, Zhang H, et al. Accelerating redox kinetics by ZIF-67 derived amorphous cobalt phosphide electrocatalyst for high-performance lithium-sulfur batteries. *Energy Mater* 2023;3:300001. DOI
3. Zhou G, Tian H, Jin Y, et al. Catalytic oxidation of Li₂S on the surface of metal sulfides for Li-S batteries. *Proc Natl Acad Sci USA* 2017;114:840-5. DOI PubMed PMC
4. Wang T, He J, Cheng X, Zhu J, Lu B, Wu Y. Strategies toward high-loading lithium-sulfur batteries. *ACS Energy Lett* 2023;8:116-50. DOI
5. Wu Q, Zhou X, Xu J, Cao F, Li C. Adenine derivative host with interlaced 2D structure and dual lithiophilic-sulfiphilic sites to enable high-loading Li-S batteries. *ACS Nano* 2019;13:9520-32. DOI
6. Wu Q, Yao Z, Zhou X, Xu J, Cao F, Li C. Built-in catalysis in confined nanoreactors for high-loading Li-S batteries. *ACS Nano* 2020;14:3365-77. DOI PubMed
7. He M, Li X, Yang X, et al. Realizing solid-phase reaction in Li-S batteries via localized high-concentration carbonate electrolyte. *Adv Energy Mater* 2021;11:2101004. DOI
8. Lin Y, Huang S, Zhong L, et al. Organic liquid electrolytes in Li-S batteries: actualities and perspectives. *Energy Stor Mater* 2021;34:128-47. DOI
9. Fan Y, Yang Z, Hua W, et al. Functionalized boron nitride nanosheets/graphene interlayer for fast and long-life lithium-sulfur batteries. *Adv Energy Mater* 2017;7:1602380. DOI
10. Fan Y, Liu D, Rahman MM, et al. Repelling polysulfide ions by boron nitride nanosheet coated separators in lithium-sulfur batteries. *ACS Appl Energy Mater* 2019;2:2620-8. DOI
11. Guo Y, Wu P, Zhong H, et al. Prussian blue analogue/KB-derived Ni/Co/KB composite as a superior adsorption-catalysis separator modification material for Li-S batteries. *J Colloid Interface Sci* 2022;625:425-34. DOI
12. Li W, Huang M, Li Y, Li C. CoS₂ as cathode material for magnesium batteries with dual-salt electrolytes (in Chinese). *J Inorg Mater* 2022;37:173. DOI
13. Li R, He J, Lei M, Yang M, Li C. High-density catalytic heterostructures strung by buried-in carbon tube network as monolithic holey host for durable Li-S batteries. *Chem Eng J* 2022;446:137294. DOI
14. Ruan J, Sun H, Song Y, et al. Constructing 1D/2D interwoven carbonous matrix to enable high-efficiency sulfur immobilization in Li-S battery. *Energy Mater* 2022;1:100018. DOI
15. Wu Q, Zhou X, Xu J, Cao F, Li C. Carbon-based derivatives from metal-organic frameworks as cathode hosts for Li-S batteries. *J Energy Chem* 2019;38:94-113. DOI
16. Li Z, Xiao Z, Wang S, Cheng Z, Li P, Wang R. Engineered interfusion of hollow nitrogen-doped carbon nanospheres for improving electrochemical behavior and energy density of lithium-sulfur batteries. *Adv Funct Mater* 2019;29:1902322. DOI
17. Wu Q, Shadik Z, Xu J, Cao F, Li C. Integrated reactor architecture of conductive network and catalytic nodes to accelerate polysulfide conversion for durable and high-loading Li-S batteries. *Energy Stor Mater* 2023;55:73-83. DOI
18. Qi X, Huang L, Luo Y, Chen Q, Chen Y. Ni₃Sn₂/nitrogen-doped graphene composite with chemisorption and electrocatalysis as advanced separator modifying material for lithium sulfur batteries. *J Colloid Interface Sci* 2022;628:896-910. DOI
19. Li R, Zhou X, Shen H, Yang M, Li C. Conductive holey MoO₂-Mo₃N₂ heterojunctions as job-synergistic cathode host with low surface area for high-loading Li-S batteries. *ACS Nano* 2019;13:10049-61. DOI
20. Shi N, Xi B, Liu J, et al. Dual-functional NbN ultrafine nanocrystals enabling kinetically boosted lithium-sulfur batteries. *Adv Funct Mater* 2022;32:2111586. DOI
21. Ma F, Zhang X, Sriniva K, et al. NbN nanodot decorated N-doped graphene as a multifunctional interlayer for high-performance lithium-sulfur batteries. *J Mater Chem A* 2022;10:8578-90. DOI
22. Zhang H, Dai R, Zhu S, Zhou L, Xu Q, Min Y. Bimetallic nitride modified separator constructs internal electric field for high-performance lithium-sulfur battery. *Chem Eng J* 2022;429:132454. DOI
23. Chen JG. Carbide and nitride overlayers on early transition metal surfaces: preparation, characterization, and reactivities. *Chem Rev* 1996;96:1477-98. DOI PubMed
24. Li R, Peng H, Wu Q, et al. Sandwich-like catalyst-carbon-catalyst trilayer structure as a compact 2D host for highly stable lithium-sulfur batteries. *Angew Chem Int Ed* 2020;59:12129-38. DOI
25. Li X, Gao B, Huang X, et al. Conductive mesoporous niobium nitride microspheres/nitrogen-doped graphene hybrid with efficient polysulfide anchoring and catalytic conversion for high-performance lithium-sulfur batteries. *ACS Appl Mater Interfaces* 2019;11:2961-9. DOI
26. Hu J, Tian J, Li C. Nanostructured carbon nitride polymer-reinforced electrolyte to enable dendrite-suppressed lithium metal batteries. *ACS Appl Mater Interfaces* 2017;9:11615-25. DOI PubMed
27. Liu J, Zhang Y, Zhang L, Xie F, Vasileff A, Qiao SZ. Graphitic carbon nitride (g-C₃N₄)-derived N-rich graphene with tuneable interlayer distance as a high-rate anode for sodium-ion batteries. *Adv Mater* 2019;31:e1901261. DOI
28. Brunauer S, Emmett PH, Teller E. Adsorption of gases in multimolecular layers. *J Am Chem Soc* 1938;60:309-19. DOI
29. Zhou X, Tian J, Wu Q, Hu J, Li C. N/O dual-doped hollow carbon microspheres constructed by holey nanosheet shells as large-grain cathode host for high loading Li-S batteries. *Energy Stor Mater* 2020;24:644-54. DOI

30. Castillo J, Qiao L, Santiago A, et al. Perspective of polymer-based solid-state Li-S batteries. *Energy Mater* 2022;2:200003. DOI
31. Wu Q, Yao Z, Du A, et al. Oxygen-defect-rich coating with nanoporous texture as both anode host and artificial SEI for dendrite-mitigated lithium-metal batteries. *J Mater Chem A* 2021;9:5606-18. DOI
32. Fan FY, Carter WC, Chiang YM. Mechanism and kinetics of Li_2S precipitation in lithium-sulfur batteries. *Adv Mater* 2015;27:5203-9. DOI PubMed
33. Chen CY, Peng HJ, Hou TZ, et al. A quinonoid-imine-enriched nanostructured polymer mediator for lithium-sulfur batteries. *Adv Mater* 2017;29:1606802. DOI
34. Li Z, Zhou Y, Wang Y, Lu Y. Solvent-mediated Li_2S electrodeposition: a critical manipulator in lithium-sulfur batteries. *Adv Energy Mater* 2019;9:1802207. DOI
35. Li L, Pascal TA, Connell JG, et al. Molecular understanding of polyelectrolyte binders that actively regulate ion transport in sulfur cathodes. *Nat Commun* 2017;8:2277. DOI PubMed PMC
36. Yang Q, Hu J, Meng J, Li C. C-F-rich oil drop as a non-expendable fluid interface modifier with low surface energy to stabilize a Li metal anode. *Energy Environ Sci* 2021;14:3621-31. DOI
37. Huang X, Wang Z, Knibbe R, et al. Cyclic voltammetry in lithium-sulfur batteries -challenges and opportunities. *Energy Technol* 2019;7:1801001. DOI
38. Luo C, Liang X, Sun Y, et al. An organic nickel salt-based electrolyte additive boosts homogeneous catalysis for lithium-sulfur batteries. *Energy Stor Mater* 2020;33:290-7. DOI
39. Feng Y, Zu L, Yang S, et al. Ultrahigh-content Co-P cluster as a dual-atom-site electrocatalyst for accelerating polysulfides conversion in Li-S batteries. *Adv Funct Mater* 2022;32:2207579. DOI
40. Helen M, Reddy MA, Diemant T, et al. Single step transformation of sulphur to $\text{Li}_2\text{S}_2/\text{Li}_2\text{S}$ in Li-S batteries. *Sci Rep* 2015;5:12146. DOI PubMed PMC
41. Wu Y, Momma T, Ahn S, Yokoshima T, Nara H, Osaka T. On-site chemical pre-lithiation of S cathode at room temperature on a 3D nano-structured current collector. *J Power Sources* 2017;366:65-71. DOI
42. Kresse G, Furthmüller J. Efficient iterative schemes for ab initio total-energy calculations using a plane-wave basis set. *Phys Rev B* 1996;54:11169-86. DOI